In Situ Engineering of the Electrode-Electrolyte Interface for Stabilized Over-lithiated Cathodes

*Tyler Evans,[1,2] Daniela Molina Piper,[2] Huaxing Sun,[3] Timothy Porcelli,[3] Seul Cham Kim,[4] Sang Sub Han,[4] Yong Seok Choi,[4] Chixia Tian,[5] Dennis Nordlund,[6] Marca M. Doeff,[5] Chunmei Ban,[7] Sung-Jin Cho,[8] Kyu Hwan Oh,[4] and Se-Hee Lee [1,]**

[1] Department of Mechanical Engineering, University of Colorado at Boulder, Boulder, Colorado 80309, USA

[2] SiILion, Inc., Broomfield, CO 80020, USA

[3] Department of Chemistry, University of Colorado at Boulder, Boulder, Colorado 80309, USA

[4] Department of Material Science and Engineering, Seoul National University, Seoul, 151-742, Korea

[5] Energy Storage and Distributed Resources Division, Lawrence Berkeley National Laboratory, Berkeley, CA 94720, USA

[6] Stanford Synchrotron Radiation Lightsource, SLAC National Accelerator Laboratory, Menlo Park, California 94025, USA.

[7] Center of Chemical and Materials Science, National Renewable Energy Laboratory, Golden, CO 80401, USA

[8] Joint School of Nanoscience and Nanoengineering, North Carolina A&T State University, Greensboro, NC 27411, USA

* Corresponding author: Professor Se-Hee Lee

E-mail: sehee.lee@colorado.edu

Abstract

Boasting high voltage operation with capacities exceeding 250 mAh g^{-1}, lithium-manganese-rich (LMR) cathodes were once considered the key to enabling a market-viable electric vehicle. Worldwide research has struggled to enable the LMR material due to its signature drawbacks: oxygen evolution and the gradual lowering of cell operating voltage over cycling life. The present study approaches LMR with an explicit focus on the cathode-electrolyte interface (CEI). We developed a modified ionic liquid electrolyte capable of forming a favorable CEI, demonstrating the highest degree of voltage fade mitigation to-date. We investigated the CEI formed on the LMR surface and demonstrated its unprecedented ability to stabilize the LMR crystal structure using a comprehensive suite of characterization methodology. Our study culminates in the first-ever demonstration of stabilized Si/LMR full-cells, capable of retaining >90% energy over early cycling and >90% capacity over more than 750 cycles at the 1C rate (100% depth-of-discharge).

At the turn of the 21st century, scientists were working hard to develop a lithium-ion (Li-ion) cathode technology that would change the way people viewed energy storage. A newly developed cathode material had the potential to revolutionize the transportation industry, especially if the material could be paired with a high capacity anode material such as silicon (Si). The silicon/high-energy cathode full-cell was proposed to truly enable the electric vehicle (EV), driving down battery costs to less than $200/kWh while supplying double the drive range of state-of-the-art Li-ion technology. The material, formulated as $x\mathrm{Li_2MnO_3}\bullet(1\text{-}x)\mathrm{LiMO_2}$ or $\mathrm{Li[Li_xM_{1-x}]O_2}$ (M = Ni, Mn, Co), is known as the lithium-manganese-rich (LMR) oxide.

While the true theoretical capacities of layered intercalation cathode materials are about 280 mAh g^{-1}, surface reactivity and instabilities at high states of charge limit the practical capacities of traditional layered cathode materials such as $\mathrm{LiCoO_2}$ (~140 mAh g^{-1}) and $\mathrm{LiNi_{1/3}Mn_{1/3}Co_{1/3}O_2}$ (about 160 mAh g^{-1}).[1] The beauty of the LMR material lies in the activation process undergone at >4.4 V vs. $\mathrm{Li/Li^+}$ during initial charging, resulting in an unprecedentedly high operating voltage and capacities of ~260 mAh g^{-1}.[2-7] The LMR cathode material gained the world's attention with the potential to double the energy density of the world's best Li-ion systems.

Despite these advantages and the potential for massive technological impact, worldwide research has struggled to enable the LMR material. Early work impressively laid the foundation for widespread efforts targeting this material and its signature drawback: the gradual lowering of cell operating voltage over cycling life as the originally layered crystal structure transforms to a spinel phase, accompanied by oxygen evolution during activation of the $\mathrm{Li_2MnO_3}$ component and transition metal dissolution. The practical issue arising from this voltage fade is the continuous alteration of cell energy associated with a given state of charge over the cycle life of the LMR material, leading to a failure to satisfy the performance requirements of any application requiring constant power and energy throughout operation.

The pristine LMR oxide structure has been described as either a composite of O3 oxygen stacked layered trigonal $\mathrm{LiMO_2}$ (R-3*m* space group) and monoclinic $\mathrm{Li_2MnO_3}$ (C2/*m* space group) phases or as a solid solution.[2,8-11] During initial cycling of the LMR material, the material undergoes transformation ("activation") by which lithium and oxygen are concomitantly extracted from the lattice, accompanied by the generation of oxygen vacancies and the migration of Mn ions into the newly formed vacancies. Throughout cycling, the LMR material further exhibits a transformation from a layered structure to a defect spinel, initially forming a surface reconstruction layer (SRL) which progressively grows inwards from particle edge to bulk during

cycling.[9-11] The drastic structural changes of the LMR material can generally be understood as 1) an initial activation with concurrent oxygen loss from the originally layered lattice followed by the parallel effects of 2) TM cations filling Li sites upon discharge with simultaneous dissolution of TM ions (most significantly Mn^{2+}) and 3) reduction of TM cations to lower valence states.[1-11] The result of these structural changes is the loss of Li intercalation sites and the formation of a spinel phase (F*d*-3*m* space group) with a significantly lower operating voltage compared to that of the initial layered material, with the changes becoming more severe with cycling. In an attempt to alleviate oxygen evolution and mitigate phase transformation in the LMR material, myriad efforts have focused on surface modification,[12-13] ion substitution or doping,[14-17] and morphological control of particles and grains,[18-20] all with limited success in enhancing long term cell energy retention.

With the pressure mounting for the development of the next-generation Li-ion cathode system, the LMR material remains the subject of intensified research efforts. As the Li-ion industry is already commercializing Si materials in various anode composite structures while making major strides to enable pure Si nano-structures, the heat is on to perfect a high-energy cathode capable of matching these new high capacity anode systems. In this work, we focus our efforts on the electrode-electrolyte interactions known to accelerate phase change in the LMR system. Leveraging the understandings of LMR interfacial behavior built by decades of research, we employ a unique electrolyte composition to form a cathode-electrolyte interface (CEI) that allows for the improved long-term voltage stability of the LMR cathode. Our novel CEI is formed *in situ* through the oxidative decomposition of a room temperature ionic liquid (RTIL) electrolyte doped with a sacrificial fluorinated salt additive. For the first time, we demonstrate an LMR system capable of 1000 high capacity cycles with minimal voltage decay, shedding light on the importance of the LMR CEI and elucidating the complex interplay between the electrolyte and the atomic scale transformations of an unstable crystal lattice.

Preliminary Electrochemical Performance Observations

We start by identifying and addressing the detrimental side reactions known to occur at high voltages between conventional, carbonate-based electrolytes and the LMR surface. While commonly neglected in order to focus attention on bulk material phenomena, these side reactions play a pivotal role in both the short- and long-term performance of the LMR material. Most notoriously, the formation of H^+ via the oxidative decomposition of alkyl carbonate electrolytes leads to exacerbation of phase change by promoting the disproportionation of TM valence states within the LMR crystal lattice through the charge compensation mechanism required for the reaction of $2Mn^{3+}$ to Mn^{2+} and Mn^{4+} (a.k.a. Hunter's redox mechanism).[21-24] In other words, oxidation of Mn in the LMR material occurs in parallel to partial TM dissolution and phase change due to interactions with the carbonate electrolyte. It was hypothesized that utilizing an electrolyte that forms more favorable decomposition products, ideally avoiding parasitic acid attack, would provide for a higher degree of reversibility in the electrochemical cycling of the layered LMR structure. Simply removing the conventional organic electrolyte system and replacing it with an imide-based RTIL induces impressive cycling performance, as shown in **Figure 1**. The electrochemical performance of LMR half-cells containing the material, $(0.25)Li_2MnO_3 \bullet (0.75)LiNi_{0.3}Co_{0.15}Mn_{0.55}O_2$, was compared using a conventional, carbonate-based electrolyte, a 50/50 vol. mixture of ethylene carbonate/ diethyl carbonate (EC/DEC) with 1*M* $LiPF_6$ salt, and a high performance RTIL electrolyte, N-methyl-N-propylpyrrolidinium/bis(fluorosulfonyl)imide (PYR_{13}^+/FSI^-) with 1.2*M* LiFSI salt. As expected,

the LMR cycled in carbonate-based electrolyte degrades steadily. This degradation manifests itself in capacity loss (Fig. 1c, grey profile) and evolution of the discharge voltage trace, with the high voltage plateaus displaying marked fade within just 100 cycles (Fig. 1a). Contrastingly, the LMR half-cell cycled in PYR_{13}^+/FSI^- (1.2*M* LiFSI) electrolyte maintains high capacities throughout 1000 cycles (75% capacity retention over 980 cycles at 1C-rate, red profile in Fig. 1c), with significant capacity delivered above 3.0 V vs. Li/Li^+ (55% capacity delivered above 3.0 V on 500th discharge, Fig. 1b). The relatively high operating voltage of this half-cell suggests more retention of the layered crystal phase, as the manganese-oxide spinel's redox chemistry occurs below 3.0 V vs. Li/Li^+ (Mn^{4+} reduction at ~2.8 V).[17] While simply employing an FSI-based RTIL electrolyte does not alleviate voltage fade to commercially attractive levels, these results suggest the ability of an electrolyte to significantly hinder energy decay and imply a higher degree of phase stability in the LMR material. Also of note are the low charge-transfer resistances found throughout cycling in an FSI-based RTIL, suggesting a thin, robust, and favorable CEI (**Figure S1**). The poor interfacial behavior in conventional electrolyte is further exemplified by the destruction of LMR particles after 1000 cycles, shown in Figure S1, as compared to those cycled in FSI-based RTIL which maintain their spherical morphology; this is believed to be a consequence of H^+ attack by EC/DEC breakdown products, lattice breakdown, and vacancy condensation upon delithiation.

Suppressed Long-Term LMR Phase Transformation in an Un-optimized RTIL Electrolyte

In order to confirm and further study the magnitude of phase change occurring when employing a PYR_{13}^+/FSI^- (1.2*M* LiFSI) electrolyte, we turn to X-ray diffraction (XRD) and Raman spectroscopy. **Figure 2a** and **2b** provide XRD spectra for $(0.25)Li_2MnO_3\bullet(0.75)LiNi_{0.3}Co_{0.15}Mn_{0.55}O_2$ half-cells cycled in conventional, carbonate-based electrolyte and PYR_{13}^+/FSI^- (1.2*M* LiFSI), respectively. Interestingly, both samples show similar short-term phase evolution: after just 5 cycles the (020) plane reflection at ~21 (2θ) disappears (insets in Fig. 2a and 2b), indicating a loss of layered order and TM rearrangement in the Li_2MnO_3 superlattice, while splitting of the (104) peak at ~45° (2θ) indicates formation of a defect cubic-spinel (F*d*-3*m*).[1,8,9,16] Despite these similarities in XRD peak evolution during early cycling (cycles 1-50), after 1000 cycles the LMR sample cycled in carbonate-electrolyte exhibits much more severe peak shifting and broadening, indicating a loss of long-range order and significant destruction of the original layered crystal.

To more clearly study the electrolyte-crystal phase relationship during early cycling, Figure 2c and 2d present Raman spectra evolution compared between carbonate and RTIL electrolytes. The spectrum of the pristine LMR material exhibits a weak band at ~431 cm^{-1}, indicating the metal-oxygen vibration of monoclinic Li_2MnO_3 (C2/*m*), and two broad peaks at ~481 cm^{-1} and ~593 cm^{-1}, characteristic of the vibration of oxygen atoms on the *ab*-axis (E_g and A_{1g} modes, respectively) in the layered $LiMO_2$ lattice (R-*3*m).[16,25] The broadening and splitting of the A_{1g} peak into two broad A_{1g} bands (~593 cm^{-1} and ~625 cm^{-1}) is attributed to an increase in concentration of the defect spinel phase and loss of TM layered-order.[25] This affect is much more pronounced in the LMR sample cycled in carbonate electrolyte, confirming significantly lower surface concentrations of defect spinel during early cycling in RTIL electrolyte. The shown XRD and Raman characterization suggests that a FSI-based RTIL electrolyte is capable of significantly retarding LMR phase change during early cycling while providing marked stabilization of the LMR lattice over long-term cycling.

High Performance LMR Enabled by a Modified-RTIL

Despite inducing the best long-term performance demonstrated, to-date, in an LMR half-cell, the PYR_{13}^+/FSI^- (1.2*M* LiFSI) electrolyte alone does not enable truly viable levels of energy retention. Previous reports suggest that F-ion doping of the LMR particle surface[4,15-17] and utilization of fluorinated electrolyte co-solvents such as fluoroethylene carbonate (FEC) boost energy retention and rate performance.[25-28] For example, F-ion doping has been shown to reduce the deintercalation barrier of Li^+ from the LMR lattice by weakening the Li-O bond, allowing for better high rate performance and more efficient activation.[16] Most significantly, the presence of F^- alters the material's electronic environment and prohibits the mobility of oxygen ions, leading to a decrease in activation of Li_2MnO_3, which in turn can suppress phase transition as large amounts of interstitial vacancies serve as a driving force for TM migration.[4,9,17,29-32] Stronger M-F bonds also mitigate TM migration.[17] Motivated by Kang and Thackeray's early work in forming fluorinated passivation layers on the LMR surface prior to electrode fabrication,[33,34] we began searching for electrolyte additives capable of forming similar CEIs *in situ* via oxidative decomposition at high voltages. While fluorinated linear carbonates such as FEC were not successful in hindering voltage fade in our LMR-RTIL system, as shown in **Figure S2** (see *Supporting Information* for a detailed discussion of FEC addition), we found surprising and impressive success in mitigating phase change by adding the well-known $LiPF_6$ salt – modification of the RTIL electrolyte using $LiPF_6$ provides world-record LMR performance. As shown in **Figure 3**, adding small concentrations (0.1*M* and higher) of $LiPF_6$ to the PYR_{13}^+/FSI^- (1.2*M* LiFSI) electrolyte (Figure 3b) drastically improves $(0.25)Li_2MnO_3•(0.75)LiNi_{0.3}Co_{0.15}Mn_{0.55}O_2$ half-cell energy retention (Figure 3c, >70% energy retention in 950 cycles at C/2 rate vs. <50% energy retention in un-modified RTIL). To our knowledge, this is the first time that the voltage profile shape of the LMR material has been maintained for 1000 cycles with >60% discharge capacity provided at voltages above 3.0 V vs. Li/Li^+ upon 1000th discharge (Figure 3a). **Figure S3** provides a direct comparison between 200th cycle voltage profiles of LMR electrodes cycled in EC/DEC, RTIL, and modified RTIL (*m*-RTIL) electrolytes, along with a performance comparison of the $(0.25)Li_2MnO_3•(0.75)LiNi_{0.3}Co_{0.15}Mn_{0.55}O_2$ material in the *m*-RTIL and organic electrolytes under ANL's "Voltage Fade Testing Protocol" (v1),[35] and **Figure S4** provides a direct comparison to state-of-the-art efforts using an upper cut-off voltage of 4.5 V. These results highlight the energy retention in the *m*-RTIL. Figure S3 also demonstrates the more efficient "activation" in *m*-RTIL, with a first cycle coulombic efficiency (CE_1) of 91.92%, compared to that in conventional electrolyte (CE_1=76.04%), corroborating previous research which argues that fluorinated LMR surfaces can enable more energy efficient material activation.[16,25,27] This unprecedented cycling performance clearly demonstrates the ability of specific RTIL-salt combinations to hinder phase change in the LMR material to commercially viable levels, stabilizing the LMR lattice and providing groundbreaking energy and capacity retention. Further evidence of LMR phase stability in the *m*-RTIL electrolyte is provided by the rate study in **Figure S5**; after an initial rate test and 50 cycles at the rate of 1C, the LMR sample cycled in the *m*-RTIL electrolyte maintains its high-rate capacities while the sample cycled in conventional electrolyte shows significant capacity fade at each rate tested. The degradation in rate performance in conventional electrolyte is attributed to the formation of a poor, resistive CEI and the loss of Li^+ vacancies and blocking of Li^+ diffusion channels via the formation of spinel regions within the LMR composite.[36]

Interfacial Chemistry and Mechanistic Details

The primary finding discussed in this paper is the ability of a novel electrolyte composition to form a LMR phase-stabilizing CEI upon oxidative decomposition during electrochemical cycling. After demonstrating the ability of our electrolyte composition to enable long-term energy retention in LMR half-cells, it is of utmost importance to develop an accurate physical depiction of this interface. **Figure 4** presents the X-ray photoelectron spectroscopy (XPS) study of the CEI's chemical make-up after cycling in each electrolyte. The XPS depth profiling of fluorine content present through the LMR-electrolyte interface demonstrates the ability of the $PYR_{13}FSI$ (1.2*M* LiFSI, 0.1*M* $LiPF_6$) electrolyte to create a heavily fluorinated CEI *in situ* (during electrochemical cycling), showing increasing fluorine content with proximity to the LMR surface (Figure 4d). This indicates the sacrificial nature and preferential decomposition of the $LiPF_6$ additive at high voltages (see *Supporting Information* for full compositional XPS depth profiling of the interfaces formed in each electrolyte, **Figure S6**). Of high importance is the evidence of TMs (Ni, Mn) throughout the CEI formed in conventional electrolyte (Figure 4a and Figure S5). Contrastingly, TM traces do not appear in the CEI formed in *m*-RTIL until 40 nm depth (Figure S5). This is indicative of a much higher degree of TM leaching in conventional electrolyte as compared to *m*-RTIL and also suggests a relatively thin, 40-80 nm thick CEI formed in the optimized RTIL electrolyte (the CEI formed in conventional electrolyte was found to be >150 nm thick). The XPS spectra deconvolutions provided in Figure 4a-c display the molecular constituents found on the CEIs formed in each electrolyte tested, with LiF found in electrolytes containing the $LiPF_6$ salt. While the CEIs formed in both *m*-RTIL and conventional electrolytes contain significant contents of favorable fluorinated compounds (LiF), the parasitic byproducts of EC and DEC breakdown likely attack the LMR surface and exacerbate phase transformation and TM dissolution.[21-24] The mechanisms of degradation in carbonate electrolytes override the beneficial effects of the $LiPF_6$ salt. H^+ formation in the organic electrolyte is inferred by the formation of C-F bonds found in the CEI of the sample cycled in EC/DEC (1*M* $LiPF_6$) electrolyte. Based on this interfacial characterization, we conclude that we induce favorable LMR/*m*-RTIL interfacial behavior through the *in situ* formation of a heavily fluorinated interface, leveraging the electrochemical properties of a high voltage RTIL-based electrolyte and the chemical interplay between the LMR lattice and the decomposition products of a sacrificial salt additive.[25-34]

It is proposed that the formation of a fluorine-rich layer on the LMR surface when cycled in *m*-RTIL contributes to the stabilization of TM ions with in the LMR particle. In order to further confirm the impact of *m*-RTIL on the stability of the CEI, X -ray absorption spectroscopy (XAS) on L-edge Mn was collected to probe the surface chemistry of the cycled LMR electrodes. The transitions from Mn 2p orbitals to unoccupied metal 3d orbitals in the LMR lattice can be measured to indicate the local hybridization states for Mn-O octahedral units.[37] As displayed in **Figure S7**, the electronic structure of manganese has been stabilized by using the *m*-RTIL electrolyte; there are no major changes in Mn L-edge XAS for the electrodes cycled in *m*-RTIL. This is, to the knowledge of the authors, the first demonstration of TM oxidation state stabilization at the LMR surface during cycling. In contrast, the low-energy component of the Mn L-edge spectrum appears after only one cycle when using the conventional carbonate electrolyte. Minimum XAS signals were observed in the conventional carbonate electrolyte after 200 cycles, which can be attributed to the blockage by CEI (150 nm thick) left after the washing procedure and Mn dissolution or migration towards the particle core. With different configurations, L-edge XAS allows different sample depths to be measured from 1-2nm (AEY),

2-5nm (TEY) up to 50nm (FY). XAS/FY was performed on the fully discharged states of the LMR electrodes in order to understand the impact of the electrolytes on the bulk chemistry, as shown in the *Supporting Information* (**Figure S8**). Significant changes have been observed in the electrodes cycled in the carbonated electrolyte. Analysis of the FY mode Mn L-edge XAS reveals the same trend demonstrating Mn stabilization in the core of the LMR particles cycled in *m*-RTIL. The increasing intensity from the low-energy shoulders indicates that the oxidation state of Mn is reduced upon cycling. During transformation to the spinel-phase, the average Mn oxidation state shifts towards 3^+, inducing strain and lattice distortions due to the Jahn-Teller effect (Mn^{3+} is Jahn-Teller active), and this further contributes to lattice instability and layered-to-spinel phase change.[7,10,37] As the presence of highly electronegative fluorine has been shown to enable more efficient activation,[16] inhibit the mobility and loss of oxygen ions,[4,9,17,29-32] and suppress TM migration through strong M-F interactions,[17] it is likely that the highly fluorinated CEI formed in *m*-RTIL mitigates phase change and disproportionation/lowering of the Mn oxidation state.

Crystallographic Analysis of Phase Transformation

The most effective means of confirming the proposed interfacial mechanism behind the observed LMR energy retention is the direct observation of phase stability via high resolution microscopy. To investigate the physical implications of the CEI formed *in situ* between the LMR and *m*-RTIL, high resolution transmission electron microscopy (HR-TEM) was performed on electrode samples after undergoing 100 cycles in both conventional and *m*-RTIL electrolytes, as shown in **Figure 5**. HR-TEM of a pristine (un-cycled) LMR particle is shown in **Figure S9**. In both cases, a clearly defined defect layer is evident at the surfaces of the LMR particles. This layer is distinguished by obvious cation re-ordering, characteristic of the surface reconstruction layer (SRL) formed on LMR particles during early cycling in conventional electrolytes,[9,10,17,28,32,38,39] The SRLs exhibit reticulate patterns which are suggestive of the topotactic characteristics of the (111) planes of a defect-spinel phase.[40-42] This phenomenon (SRL formation) occurs as TM ions with reduced oxygen coordination become destabilized due to a reduced migration energy barrier and migrate into the Li interlayers,[9,28,39] suggesting similar activation mechanisms in both conventional and *m*-RTIL electrolytes. Differences in SRL thickness formed in these electrolytes are ascribed to reduced activation (extraction of oxygen) in the *m*-RTIL electrolyte as well as continuous surface corrosion by acidic species formed in the carbonate electrolyte.[28,36,43-45] Figure 5c and 5d present HR-TEM images of particle cores after 100 cycles in each electrolyte. Of high importance is the relative disorder found in the LMR particles cycled in conventional electrolyte; a highly irregular bulk structure is visible, likely caused by continuous attack by electrolyte decomposition byproducts and particle breakage, along with evidence of seemingly amorphous domains. As formation of spinel intergrowths dominates the bulk structure, severe strains and lattice distortion (due to the Jahn-Teller effect induced by the presence of Mn^{3+} in the spinel crystal) leads to the formation of amorphous-like regions with indistinct fast Fourier transform (FFT).[17,32,36,40]After 100 cycles in conventional electrolyte, the spinel/amorphous regions dominate both the bulk and particle edge[17,32,36,40] whereas the LMR particles cycled in *m*-RTIL retain their layered structure except at the particle edge.

This TEM analysis allows for the direct observation of increased LMR phase stability in the *m*-RTIL electrolyte. TEM imaging substantiates our previous characterization, finding activation and formation of a SRL during early cycling while showing evidence of long-term

phase stability in the bulk of the LMR particles.

Of course, the practical goal of much Li-ion cathode material research is the incorporation of long-lasting, high energy materials in a lithium-ion full-cell. Up to this point in our study, we have provided in-depth characterization of the LMR system in a *m*-RTIL electrolyte and proposed a mechanism for the observed phase stability through the *in situ* formation of a heavily fluorinated CEI. Combining this work and our recent study of the compatibility between $PYR_{13}FSI$ electrolytes and the polyacrylonitrile (PAN) coated silicon anode architecture,[46-48] we demonstrate the dual-functionality of the *m*-RTIL electrolyte in enabling both high performance Si and LMR electrodes by building Si-cPAN/*m*-RTIL/LMR lithium-ion batteries (LIBs) capable of reversible, high energy cycling for an exceptionally long cycling life (see *Methods* for details on full-cell fabrication).

Figure 6 presents the first-ever academic demonstrations of the long-term, high energy cycling of Li-ion full-cells containing a high performance Si anode and a LMR cathode. Figure 6a presents a Si-cPAN/LMR full-cell, coin-type configuration, containing >20 mg of LMR active material, representing the performance of the Si/*m*-RTIL/LMR system with commercially viable mass loadings. This cell retains >90% of its first discharge energy density at its 50^{th} discharge, proving that the early-cycling half-cell energy retention behavior depicted in Figure 3 propagates into exceptional full-cell performance. Inclusion of such a cell in this study is important to draw attention to the ability of RTIL-based electrolytes to fully wet thick, calendared electrode composites and to begin dispelling the stigmas associated with RTIL viscosity. This cell is run at the C/10 rate, and future work should certainly address limitations on RTIL conductivity. To supplement the demonstration of a non-flammable 5 mAh coin-type Si/LMR full-cell, we combine our LMR/*m*-RTIL system with the previously developed, ultra-stable nano-wire Si anode system (SiNW-cPAN).[48] This full-cell, shown in Figure 6c, maintains 90.84% capacity over more than 750 cycles at the 1C rate, leveraging both the high rate performance and stability of the SiNW-cPAN anode system and the stability of the LMR/*m*-RTIL cathode system, and retains greater than 84% capacity over 1000 cycles at various rates. This cycling performance is well within the Department of Energy Vehicle Technology Office's (DOE VTO) LIB performance requirements (>80% retention @ 1000 cycles with 80% DoD).[49]

While this study, along with previous work on the Si-RTIL system, lays the foundation for a low-volatility Si/LMR battery by demonstrating impressive full-cell performance and proposes a working mechanism for the observed cell stability, a number of technical hurdles remain. The first such hurdle lies in making conclusive statements regarding RTIL-induced phase stability. In this study, the authors prove that the *in situ* formation of a fluorinated CEI, in combination with the use of a high voltage electrolyte solvent, stabilizes the LMR lattice (reducing TM migration) and enables higher degrees of energy retention; but going deeper, the question remains: how exactly does this interface operate to reduce LMR phase change? One theory lies in the ability of the RTIL to postpone Li migration during activation; the electrolyte system may be able to provide Li ions to the LMR surface, saturating the surface and resulting in little or no migration of Li to tetrahedral interstitial sites in the LMR lattice. The authors identify this mechanism as an area of interesting future academic work. Along with the previously mentioned limitations on RTIL conductivity, future research should work to further accommodate oxygen evolution upon LMR activation while also exploring material modifications that can work in tandem with the RTIL phase stabilization mechanism to facilitate even lower levels of voltage loss. Figure 6b presents the monumental technical and societal

impact that could result from the commercialization of the Si/LMR battery; this cell could enable a high-range, affordable EV, and the utilization of an RTIL-based electrolyte would provide the major safety benefit of non-flammability. Validated by unprecedented cycling data and a thorough combination of materials- and system-level characterization, our approach to developing a stable high energy LMR-electrolyte system represents important progress towards a safer, higher-performance secondary LIB.

Methods

Electrode and Electrolyte Preparation. $(0.25)Li_2MnO_3•(0.75)LiNi_{0.3}Co_{0.15}Mn_{0.55}O_2$ active material powder was synthesized and supplied by Dr. Sung-Jin Cho at North Carolina A&T State University. $(0.25)Li_2MnO_3•(0.75)LiNi_{0.3}Co_{0.15}Mn_{0.55}O_2$and Si-cPAN electrodes were fabricated according to our procedures described in Ref. [49] and Ref. [46], respectively. Ionic liquid electrolytes were purchased from Boulder Ionics Corporation (U.S.A.) and scanned for halide impurities. Impurities (F^-, Cl^-, Br^-, SO_4^-) were quantified using a Dionex ICS-1100 chromatograph, calibrated for sensitivities as low as 1 ppm. Ion chromatography was performed on all ionic liquids and lithium salts used in this work, and the total impurity content of every solution was calculated based off the mass percentage of electrolyte component in the total mass of electrolyte. The solutions contained less than 20 ppm (w/w) of moisture and less than 10 ppm (w/w) of halide and metal-ion impurities. 1*M* $LiPF_6$ in ethylene carbonate:diethyl carbonate (50:50, Soulbrain) was used as a conventional organic electrolyte.

Electrochemical Characterization. Electrochemical measurements were carried out using an Arbin^{TM} BT2000 battery test station. All half-cells were assembled using our prepared $(0.25)Li_2MnO_3•(0.75)LiNi_{0.3}Co_{0.15}Mn_{0.55}O_2$ electrodes as the working electrode and lithium metal foil as the counter electrode. The separator was a glass micro-fiber disk (Whatman^{TM} GF/F) and the shell was a stainless steel CR2032 coin cell (Pred Materials). The electrolyte systems utilized were EC/DEC (1*M* $LiPF_6$) and $PYR_{13}FSI$ (1.2*M* LiFSI), with additives $LiPF_6$ (Sigma Aldrich), fluoroethylene carbonate (Sigma Aldrich) and others. We used a constant current (CC) testing scheme to cycle our half-cells. No voltage holds were utilized during cycling (lithiation or delithiation), preventing the currents applied to relax and supply/remove extra Li^+. The half-cells were discharged (lithiated) and charged (delithiated) with various cycling currents (where a C/10 rate is equivalent to ~150 μA cm^{-2}) between 2.5 and 4.6V (vs. Li/Li^+), with an activation cycle (first full cycle) carried out between 2.5 and 4.7V (vs. Li/Li^+) at a C/20 rate. Electrochemical measurements of half-cells were all normalized based on the mass of $(0.25)Li_2MnO_3•(0.75)LiNi_{0.3}Co_{0.15}Mn_{0.55}O_2$ active material in each electrode (typically 6 mg).

X-ray Diffraction. XRD patterns of powdered samples were collected with CuKα radiation (λ = 1.5418 Å) in the 2θ range of 10°−65°, using a Bruker AXS D2 Phaser benchtop XRD system operated at 30 kV and 30 mA. A Lynxeye XE 1D detector with a step size of 0.02° and collection time of 1 s per step were employed. Sample displacement was corrected by using a pure corundum internal standard. Prior to XRD characterization, all samples were rinsed for 5 min. in DMC solvent.

Raman Spectroscopy. Raman spectra were collected on a Jasco NRS-3100 equipped with a 532 nm laser for excitation at a power level of 22 mW. Raman scattering was dispersed by a 2400 lines/mm grating. The sample was analyzed under 100 magnification. Prior to Raman spectroscopy characterization, all samples were rinsed for 5 min. in DMC solvent.

X-ray Photoelectron Microscopy. The film composition was determined by X-ray photoelectron spectroscopy (XPS) on a PHI 5600 instrument (RBD Instruments) with a monochromatic Al Kα source (1486.6 eV). Prior to XPS characterization, all samples were cycled ten times in order to allow for CEI formation; samples were then bathed in the solvent of the respective electrolyte utilized during cycling to remove residue without destroying the CEI. Survey scans were obtained with a pass energy of 93.9 eV and a step size of 0.400 eV. Ar ion sputtering was used for depth profiling analysis with a pass energy of 29.35 eV and a step size of 0.250 eV. An electron beam neutralizer was kept on during the measurements. Data was collected with the Auger Scan software package (RBD Instruments) and analyzed by the

CasaXPS software package (Casa Software).

Morphological/ Crystallographic Characterization. FIB (FEI, NOVA200 dual beam system) equipped with a mobile air-lock chamber was used for TEM sample preparation. TEM analysis was performed with a FEI Tecnai F20 operated at 200 keV. TEM samples were prepared by section electrodes, both cycled and uncycled, using a FIB's 30 keV Ga^+ ion beam.

Full-cell fabrication. Full-cells were fabricated from pre-conditioned electrodes (as in Ref. [47] and in Ref. [48]) selected based on deliverable capacity. Calculated from the active material mass, Si-cPAN anodes were fabricated and matched with LMR cathodes such that the total anode capacity was approximately 130% of that of the cathode capacity. Both electrodes were then pre-conditioned: the anodes were allowed to run for 10 charge-discharge cycles in a half-cell configuration and were stopped after full lithiation, while the cathodes were allowed to run for 3 charge-discharge cycles in a half-cell configuration and were stopped after full delithiation. The half-cells were then disassembled and the electrodes were used to fabricate 2032 coin-cell (Al-clad cathode cup) type full-cells. This method of pre-conditioning allows for full control of the amount of lithium in the system. We used a constant current constant voltage (CCCV) testing scheme to cycle our full-cells. The full-cells were discharged and charged with various cycling currents between 1.5 and 4.55V (vs. Li/Li^+), with an activation cycle (first full cycle) carried out between 2.5 and 4.65V (vs. Li/Li^+) at a C/20 rate. Electrochemical measurements of full-cells were all normalized with respect to total mass of electro-active material in both cathode and anode electrodes.

Acknowledgments

This work was supported by a grant from the National Science Foundation (NSF, DMR-1206462). The work at NREL was supported by the Assistant Secretary for Energy Efficiency and Renewable Energy, Office of Vehicle Technologies of the U.S. Department of Energy under Contract No. DE-AC-36-08GO28308 under the Applied Batteries Research (ABR) Program. The synchrotron soft XAS of this research was carried out at the Stanford Synchrotron Radiation Lightsource, a Directorate of SLAC National Accelerator Laboratory and an Office of Science User Facility operated for the US Department of Energy Office of Science by Stanford University. Use of the Stanford Synchrotron Radiation Lightsource, SLAC National Accelerator Laboratory, is supported by the US Department of Energy, Office of Science, Office of Basic Energy Sciences under Contract No. DE-AC02-76SF00515. C. T. and D.N. would like to thank J.S. Lee for his assistance at beamline 8-2 of SSRL.Any opinions, findings, and conclusions or recommendations expressed in this material are those of the author(s) and do not necessarily reflect the views of the Department of Energy.

Author Contributions

T.E. led this this work carrying out experiments, analyzing and discussing data, and writing the manuscript; D.M.P. helped organize experiments, and analyze and discuss data; H.S. and T.P. conducted the XPS study and XPS data analysis, including spectra deconvolution; S.C.K. and S.S.H. performed FIB and HRTEM under the guidance and mentoring of K.H.O.; C.B. worked with C.T., D. N.and M.M.D on analysis of structure via XAS experiments; S.-J.C. provided LMR material, discussed data, and aided in the writing of the manuscript; S.-H.L guided and mentored the study and the preparation of the manuscript.

Additional Information

Supplementary information accompanies this paper on www.nature.com. Reprints and permissions information is available online at http://npg.nature.com/reprintsandpermissions. Correspondence and requests for materials should be addressed to S.-H.L.

References

1. Yu, H. & Zhou, H. High-energy cathode materials (Li_2MnO_3-$LiMO_2$) for lithium-ion batteries. *J. Phys. Chem. Lett.* **4**, 1268-1280 (2013).
2. Thackeray, M.M. *et al.* Li_2MnO_3-stabilized $LiMO_2$ (M = Mn, Ni, Co) electrodes for lithium-ion batteries. *J. Mater. Chem.* **17**, 3112-3125 (2007).
3. Amatucci, G.G., Pereira, N., Zheng, T., & Tarascon, J.M. Failure mechanism and improvement of the elevated temperature cycling of $LiMn_2O_4$ compounds through the use of the $LiAl_xMn_{2-x}O_{4-z}F_z$ solid solution. *J. Electrochem. Soc.* **148**, A171-A182 (2001).
4. Kang, S.H. & Amine, K. Layered $Li(Li_{0.2}Ni_{0.15+0.5z}Co_{0.10}Mn_{0.55-0.5z})O_{2-z}F_z$ cathode materials for Li-ion secondary batteries. *J. Power Sources* **146**, 654-657 (2005).
5. Roussow, M.H. & Thackeray, M.M. Lithium manganese oxides from Li_2MnO_3 for rechargeable lithium battery applications. *Mater. Res. Bull.* **26**, 463-473 (1991).
6. Kalyani, P., Chitra, S., Mohan, T., & Gopukumar, S. Lithium metal rechargeable cells using Li_2MnO_3 as the positive electrode. *J. Power Sources* **80**, 103-106 (1999).
7. Croy, J. *et al.* First-cycle evolution of local structure in electrochemically activated Li_2MnO_3. *Chem. Mater.* **26**, 7091-7098 (2014).
8. Mohanty, D. *et al.* Unraveling the voltage-fade mechanisms in high-energy-density lithium-ion batteries: origin of the tetrahedral cations for spinel conversion. *Chem. Mater.* **26**, 6272-6280 (2014).
9. Boulineau, A., Simonin, L., Colin, J.F., Bourbon, C., Patoux, S. First evidence of manganese-nickel segregation and densification upon cycling in Li-rich layered oxides for lithium batteries. *Nano Lett.* **13**, 3857-3863 (2013).
10. Yan, P. *et al.* Evolution of lattice structure and chemical composition of the surface reconstruction layer in $Li_{1.2}Ni_{0.2}Mn_{0.6}O_2$ cathode material for lithium ion batteries. *Nano Lett.* **15**, 514-522 (2015).
11. Shukla, A. *et al.* Unravelling structural ambiguities in lithium- and manganese-rich transition metal oxides. *Nat. Comm.* **6**, 8711 (2015).
12. Wu, F. *et al.* Can surface modification be more effective to enhance electrochemical performance of lithium rich materials? *J. Mater. Chem.* **22**, 1489-1497 (2012).
13. Deng, H., Belharouak, I., Yoon, C.S., Sun, Y.K., Amine, K. High temperature performance of surface-treated $Li_{1.1}(Ni_{0.15}Co_{0.1}Mn_{0.55})O_{1.95}$ layered oxide. *J. Electrochem. Soc.* **157**, A1035-A1039 (2010).
14. Deng, Z.Q. & Manthiram, A. Influence of cationic substitutions on the oxygen loss and reversible capacity of lithium-rich layered oxide cathodes. *J. Phys. Chem. C.* **115**, 7097-7103 (2011).
15. Luo, Q. & Manthiram, A. Effect of low-temperature fluorine doping on the properties of spinel $LiMn_{2-2y}Li_yM_yO_{4-z}F_z$ (M = Fe, Co, and Zn) cathodes. *J. Electrochem. Soc.* **156**, A84-A88 (2009).
16. Dong, X. *et al.* Towards low-cost, high energy density Li_2MnO_3 cathode materials. *J. Mater. Chem. A* **3**, 670-679 (2014).
17. Li, L. *et al.* Retarded phase transition by fluorine doping in Li-rich layered $Li_{1.2}Mn_{0.54}Ni_{0.13}Co_{0.13}O_2$ cathode material. *J. Power Sources* **283**, 162-170 (2015).
18. Sun, Y.K., Myung, S.T., Kim, M.H., Prakash, J., & Amine, K. Synthesis and characterization of $Li[(Ni_{0.8}Co_{0.1}Mn_{0.1})_{0.8}(Ni_{0.5}Mn_{0.5})_{0.2}]O_2$ with the microscale core-shell structure as the positive electrode material for lithium batteries. *J. Am. Chem. Soc.* **127**, 13411-13418 (2005).

19. Wei, G.Z. *et al.* Crystal habit-tuned nanoplate material of $Li[Li_{1/3-2x/3}Ni_xMn_{2/3-x/3}]O_2$ for high-rate performance lithium-ion batteries. *Adv. Mater.* **22**, 4364-4367 (2010).
20. Yang, X.K. *et al.* Suppressed capacity/voltage fading of high-capacity lithium-rich layered materials via the design of heterogeneous distribution in the composition. *J. Mater. Chem. A* **2**, 3899-3911 (2014).
21. Robertson, A.D., & Bruce, P.G. Mechanism of electrochemical activity in Li_2MnO_3. *Chem. Mater.* **15**, 1984-1992 (2003).
22. Robertson, A.D., Armstrong, A.R., & Bruce, P.G. Layered $Li_xMn_{1-y}Co_yO_2$ intercalation electrodes – influence of ion exchange on capacity and structure upon cycling. *Chem. Mater.* **13**, 2380-2386 (2001).
23. Tang, W., Kanoh, H., Yang, X., & Ooi, K. Preparation of plate-form manganese oxide by selective lithium extraction from monoclinic Li_2MnO_3 under hydrothermal conditions. *Chem. Mater.* **12**, 3271-3279 (2000).
24. Moshkovich, M., Cojocaru, M., Gottlieb, H.E., & Aurbach, D. The study of the anodic stability of alkyl carbonate solutions by in situ FTIR spectroscopy, EQCM, NMR, and MS. *J. Electroanal. Chem.* **497**, 84-96 (2001).
25. Pham, H.Q. *et al.* Performance enhancement of 4.8 V $Li_{1.2}Mn_{0.525}Ni_{0.175}Co_{0.1}O_2$ battery cathode using fluorinated linear carbonate as a high-voltage additive. *J. Electrochem. Soc.* **161**, A2002-A2011 (2014).
26. Park, Y. *et al.* Investigation of solid electrolyte interface (SEI) film on $LiCoO_2$ cathode in fluoroethylene carbonate (FEC)-containing electrolyte by 2D correlation X-ray photoelectron spectroscopy (XPS). *J. Mol. Struc.* **1069**, 157-163 (2014).
27. Li, Y. *et al.* Fluoroethylene carbonate as electrolyte additive for improving the electrochemical performances of high-capacity $Li_{1.16}[Mn_{0.75}Ni_{0.25}]_{0.84}O_2$ material. *Electrochim. Acta* **168**, 261-270 (2015).
28. Markevich, E. *et al.* Fluoroethylene carbonate as an important component in electrolyte solutions for high-voltage lithium batteries: role of surface chemistry on the cathode. *Langmuir* **30**, 7414-7424 (2014).
29. Zheng, J., Wu, X., & Yang, Y. Improved electrochemical performance of $Li[Li_{0.2}Mn_{0.54}Ni_{0.13}Co_{0.13}]O_2$ cathode material by fluorine incorporation. *Electrochim. Acta* **105**, 200-208 (2013).
30. Zheng, J. *et al.* Functioning mechanism of AlF_3 coating on the Li- and Mn-rich cathode materials. *Chem. Mater.* **26**, 6320-6327 (2014).
31. Lu, Z., & Dahn, J.R. Understanding the anomalous capacity of $Li/Li[Ni_xLi_{(1/3-2x/3)}Mn_{(2/3-x/3)}]O_2$ cells using in situ X-ray diffraction and electrochemical studies. *J. Electrochem. Soc.* **149**, A815-A822 (2002).
32. Wu, Y. & Manthiram, A. Effect of Al^{3+} and F^- doping on the irreversible oxygen loss from layered $Li[Li_{0.17}Mn_{0.58}Ni_{0.25}]O_2$ cathodes. *Electrochem. Solid-State Lett.* **10**, A151-A154 (2007).
33. Kang, S.H. & Thackeray, M.M. Stabilization of $x Li_2MnO_3.(1-x)LiMO_2$ electrode surfaces (M = Mn, Ni, Co) with midly acidic, fluorinated solutions. *J. Electrochem. Soc.* **155**, A269-A275 (2008).
34. Kim, S.-M., Jin, B.-S., Lee, S.-M., & Kim, H.-S. Effects of fluorine-substitution and acid treatment on the electrochemical performances of $0.3Li_2MnO_3.0.7LiMn_{0.6}Ni_{0.25}Co_{0.15}O_2$ cathode material for Li-ion battery. *Electrochim. Acta* **171**, 35-41 (2015).
35. Abraham, D.P., Bettge, M., Li, Y., & Zhu, Y. Electrochemical characterization of voltage

fade in LMR-NMC. DOE Vehicle Technologies Program Annual Merit Review. Arlington, VA. May 2013.

36. Gu, M. *et al.* Formation of the spinel phase in the layered composite cathode used in Li-ion batteries. *ACS Nano* **7**, 760-767 (2012).

37. Hy, S. *et al.* Understanding the role of Ni in stabilizing the lithium-rich high-capacity cathode material $Li[Ni_xLi_{(1-2x)/3}Mn_{(2-x)/3}]O_2$. *Chem. Mater.* **26**, 6919-6927 (2014).

38. Boulineau, A. *et al.* Evolutions of $Li_{1.2}Mn_{0.61}Ni_{0.18}Mg_{0.01}O_2$ during the initial charge/discharge cycle studied by advanced electron microscopy. *Chem. Mater.* **24**, 3558-3566 (2012).

39. Xu, B., Fell, C.R., Chi, M., & Meng, Y.S. Identifying surface structural changes in layered Li-excess nickel manganese oxides in high voltage lithium ion batteries: A joint experimental and theoretical study. *Energy Environ. Sci.* **4**, 2223-2233 (2011).

40. Hong, J. *et al.* Structural evolution of layered $Li_{1.2}Ni_{0.2}Mn_{0.6}O_2$ upon electrochemical cycling in a Li rechargeable battery. *J. Mater. Chem.* **20**, 10179-10186 (2010).

41. Thackeray, M.M., Johnson, C.S., Vaughey, J.T., Li, N., & Hackney, S.A. Advances in manganese-oxide 'composite' electrodes for lithium-ion batteries. *J. Mater. Chem.* **15**, 2257-2267 (2007).

42. Johnson, C.S. *et al.* The significance of the Li_2MnO_3 component in 'composite' $xLi_2MnO_3.(1-x)LiMn_{0.5}Ni_{0.5}O_2$ electrodes. *Electrochem. Commun.* **6**, 1085-1091 (2004).

43. Zheng, J. *et al.* Corrosion/fragmentation of layered composite cathode and related capacity/voltage fading during cycling process. *Nano Lett.* **13**, 3824-3830 (2013).

44. Xia, Y., Zhou, Y., & Yoshio, M. Capacity fading on cycling of 4 V $Li/LiMn_2O_4$ cells. *J. Electrochem. Soc.* **144**, 2593-2600 (1997).

45. Ito, A. *et al.* Direct observation of the partial formation of a framework structure for Li-rich layered cathode material $Li[Ni_{0.17}Li_{0.2}Co_{0.07}Mn_{0.56}]O_2$ upon the first charge and discharge. *J. Power Sources* **196**, 4785-4790 (2011).

46. Molina Piper, D. *et al.* Conformal coatings of cyclized-PAN for mechanically resilient Si nano-composite anodes. *Adv. Energy Mater.* **3**, 697-702 (2013).

47. Molina Piper, D. *et al.* Stable silicon-ionic liquid interface for next-generation lithium-ion batteries. *Nat. Commun.* **6** (2015).

48. Molina Piper, D. *et al.* Optimized silicon electrode-architecture, -interface, and –micro-geometry for next-generation lithium-ion batteries. *Adv. Mater.* **28**, 188-193 (2015).

49. Electrochemical energy storage technical team roadmap. U.S. Department of Energy. *U.S. DRIVE* (2013).

50. Evans, T., Olson, J., Bhat, V., & Lee, S.-H. Effect of organic solvent addition to $PYR_{13}FSI$ + LiFSI electrolytes on aluminum oxidation and rate performance of $Li(Ni_{1/3}Mn_{1/3}Co_{1/3})O_2$ cathodes. *J. Power Sources* **265**, 132-139 (2014).

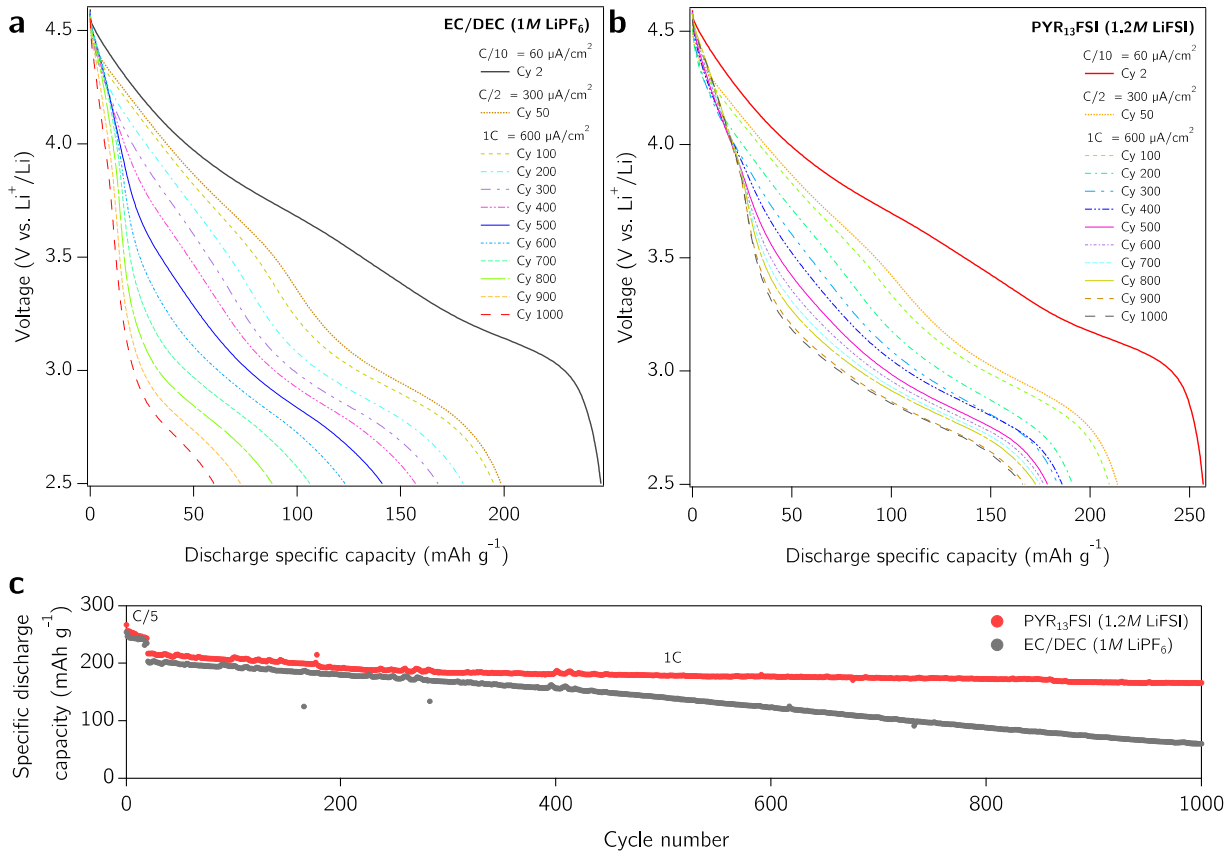

Figure 1 | Galvanostatic performance and voltage fade of the LMR electrode in conventional and RTIL electrolytes. (a) Voltage profile evolution of LMR half-cells cycled in EC/DEC (1*M* $LiPF_6$). **(b)** Voltage profile evolution of LMR half-cells cycled in $PYR_{13}FSI$ (1.2*M* LiFSI). **(c)** Specific capacities of LMR half-cells in both $PYR_{13}FSI$ (1.2*M* LiFSI) and EC/DEC (1*M* $LiPF_6$) electrolytes over 1000 cycles. Cycling was carried out at room temperature in 2032 coin-type half-cells operated between 2.5 – 4.6 V (vs. Li/Li^+) with an initial charge to 4.7 V (vs. Li/Li^+).

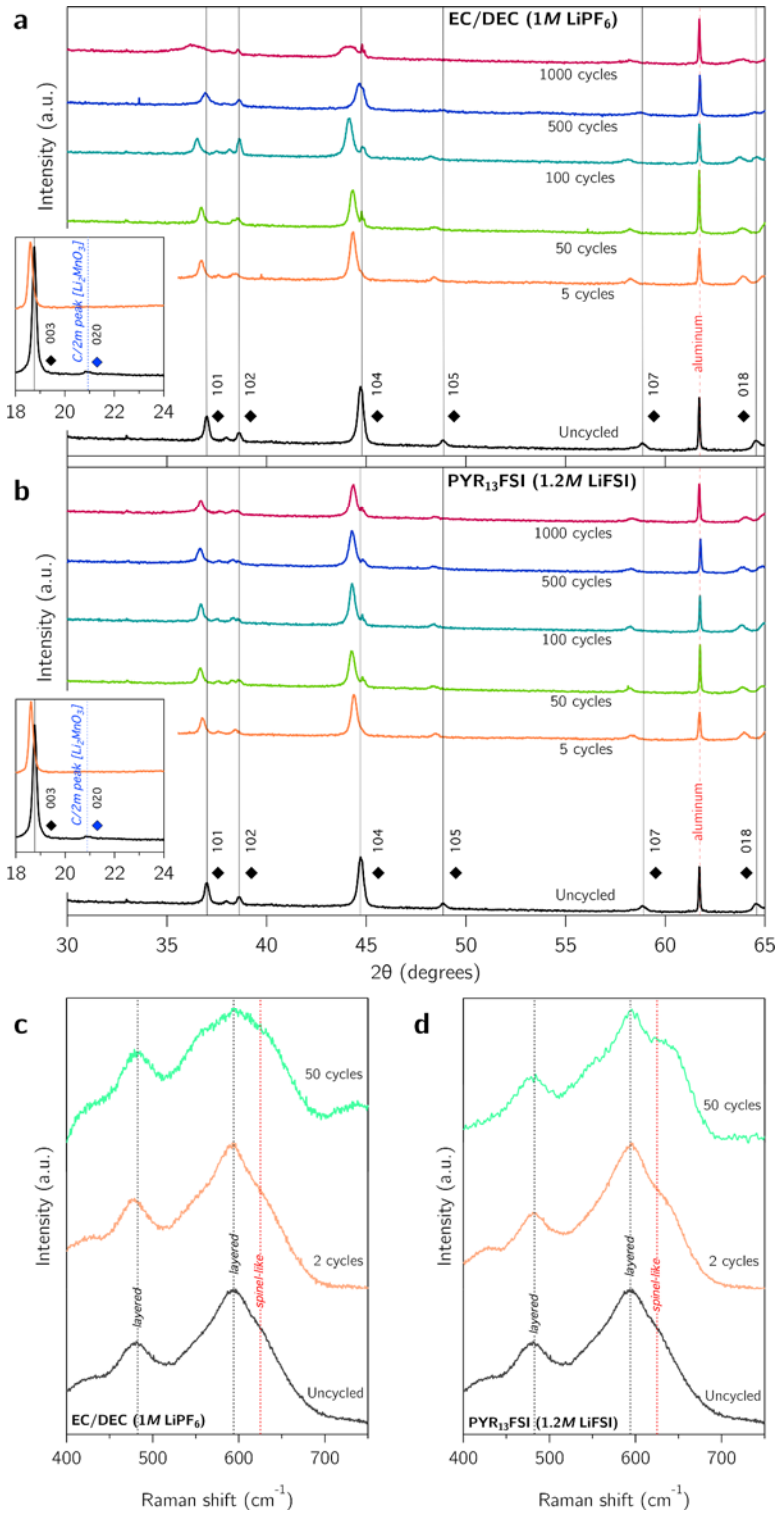

Figure 2 | LMR phase stability and crystallographic changes during cycling in conventional and RTIL electrolytes. *Ex-situ* X-ray diffraction of LMR electrodes over long-term cycling (1000 cycles) in **(a)** EC/DEC (1*M* $LiPF_6$) and **(b)** $PYR_{13}FSI$ (1.2*M* LiFSI). Insets present evolution of the Li_2MnO_3 (C2/*m*) superlattice peaks over early cycling. *Ex-situ* Raman spectroscopy of LMR electrodes over early cycling (50 cycles) in **(c)** EC/DEC (1*M* $LiPF_6$) and **(d)** $PYR_{13}FSI$ (1.2*M* LiFSI).

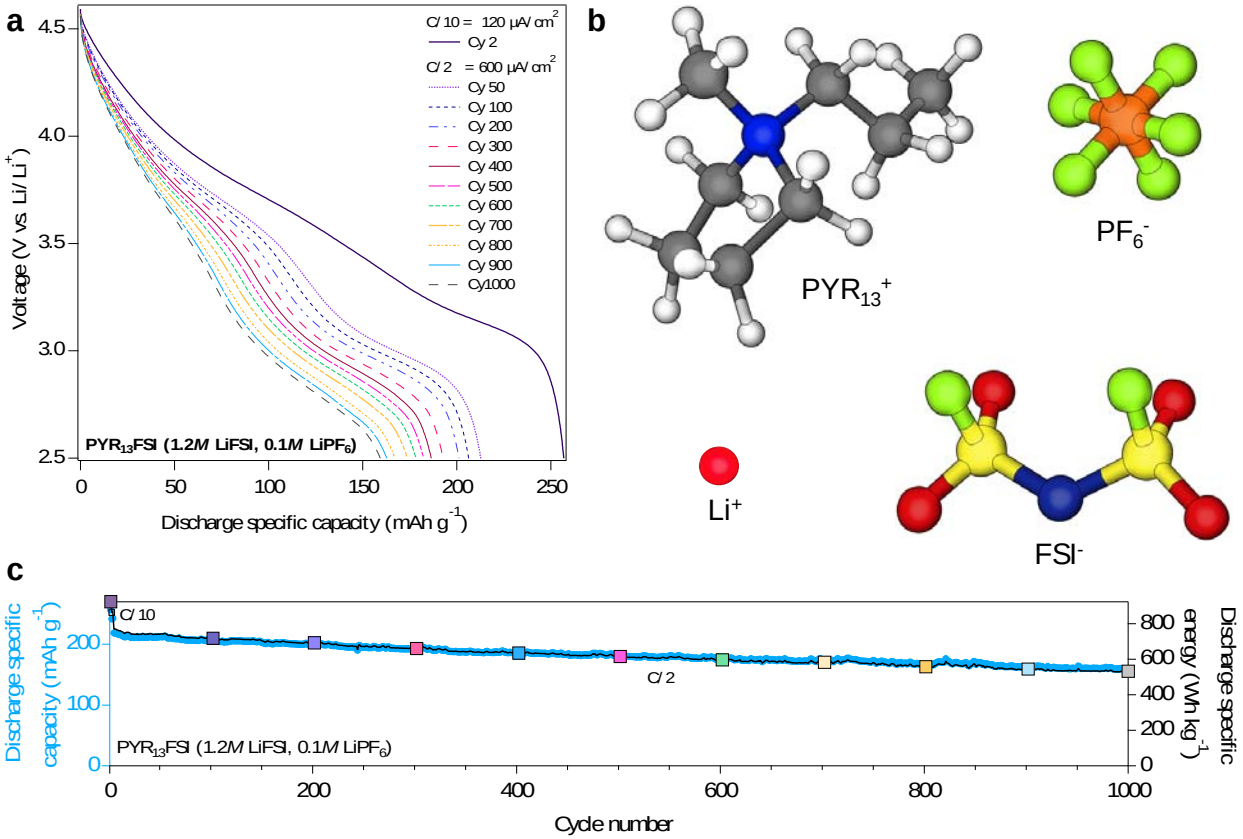

Figure 3 | Galvanostatic performance and voltage fade of the LMR electrode in an optimized RTIL electrolyte. (a) Voltage profile evolution of LMR half-cells cycled in $PYR_{13}FSI$ (1.2*M* LiFSI, 0.1*M* $LiPF_6$). **(b)** Molecular constituents of the $PYR_{13}FSI$ (1.2*M* LiFSI, 0.1*M* $LiPF_6$) electrolyte. **(c)** Specific capacity and specific energy of LMR half-cells in $PYR_{13}FSI$ (1.2*M* LiFSI, 0.1*M* $LiPF_6$) over 1000 cycles. Cycling was carried out at room temperature in 2032 coin-type half-cells operated between 2.5 – 4.6 V (vs. Li/Li^+).

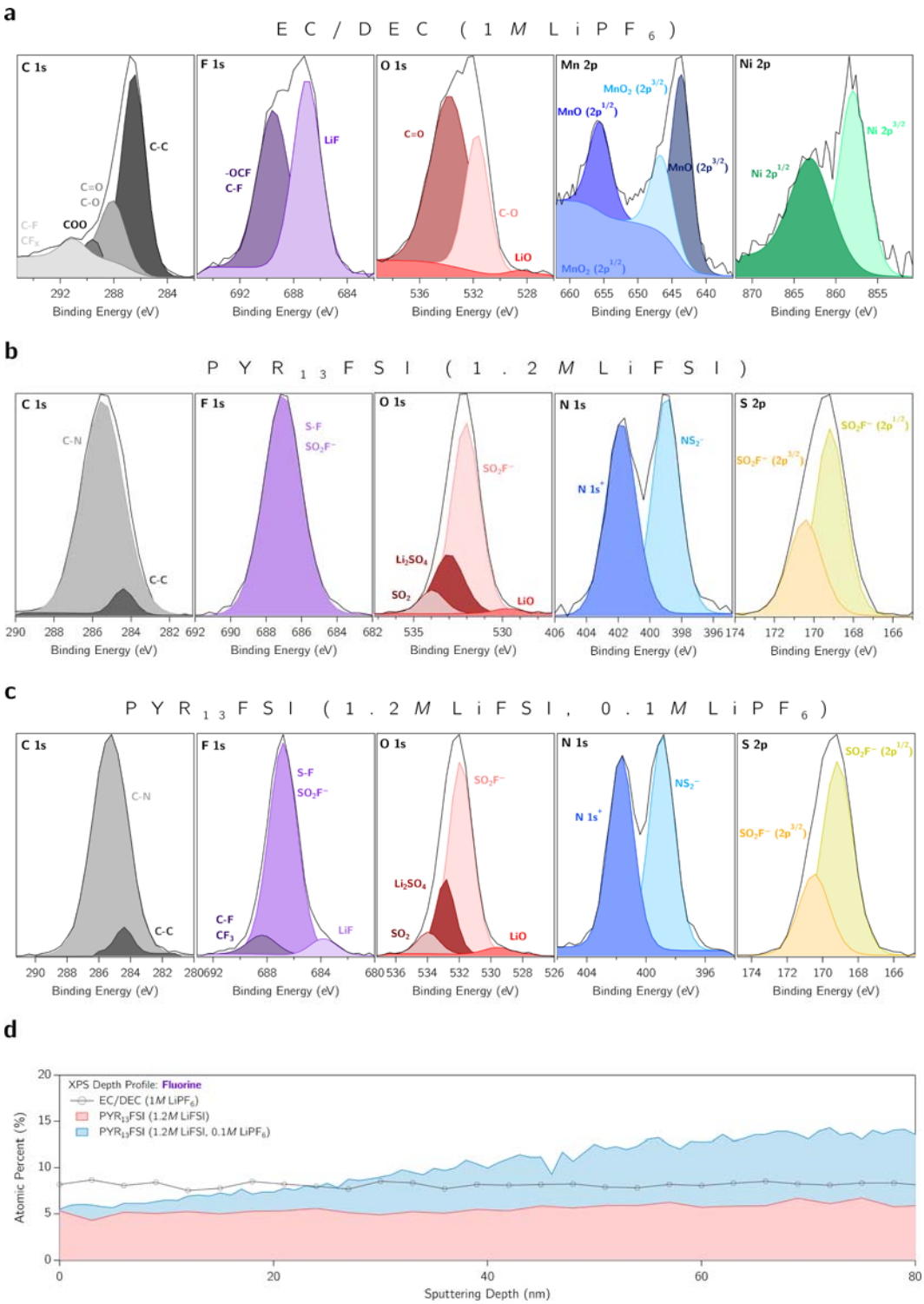

Figure 4 | Cathode-electrolyte interface composition formed in conventional and RTIL-based electrolytes. XPS analysis of the major elemental constituents forming the CEI on LMR electrodes after cycling for in **(a)** EC/DEC (1*M* $LiPF_6$) electrolyte (including carbon, fluorine, oxygen, manganese, and nickel) and **(b)** $PYR_{13}FSI$ (1.2*M* LiFSI) and **(c)** $PYR_{13}FSI$ (1.2*M* LiFSI, 0.1*M* $LiPF_6$) electrolytes (including carbon, fluorine, oxygen, nitrogen, and sulfur). **(d)** XPS depth profiling highlighting fluorine content in the CEI formed in each electrolyte.

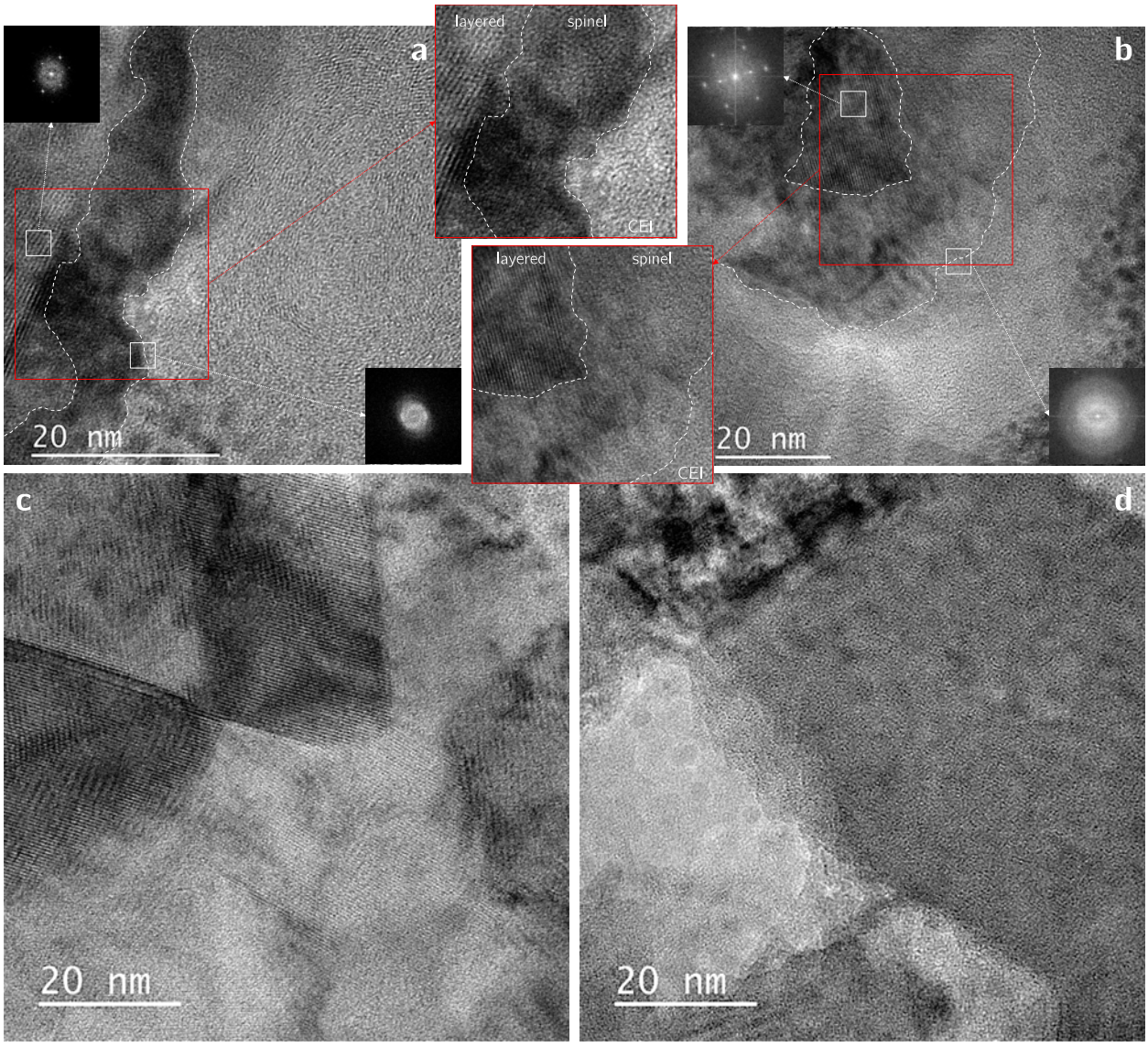

Figure 5 | Post-cycling microstructure and crystallography of LMR in conventional and *m*-RTIL electrolytes. HR-TEM showing the crystallographic and morphological effects of **(a,c)** *m*-RTIL and **(b,d)** conventional organic electrolytes on the LMR cathode material. **(a)** Micrograph of the outer edge of an LMR particle cycled 100 times in *m*-RTIL electrolyte along with fast Fourier transform (FFT) of distinct particle edge areas. **(b)** Micrograph of outer edge of an LMR particle cycled 100 times in conventional organic electrolyte along with FFT of distinct particle edge areas. **(c)** and **(d)** present HR-TEM images of particle cores after 100 cycles in *m*-RTIL and conventional electrolyte, respectively, showing the relative disorder found in the LMR particles cycled in conventional electrolyte.

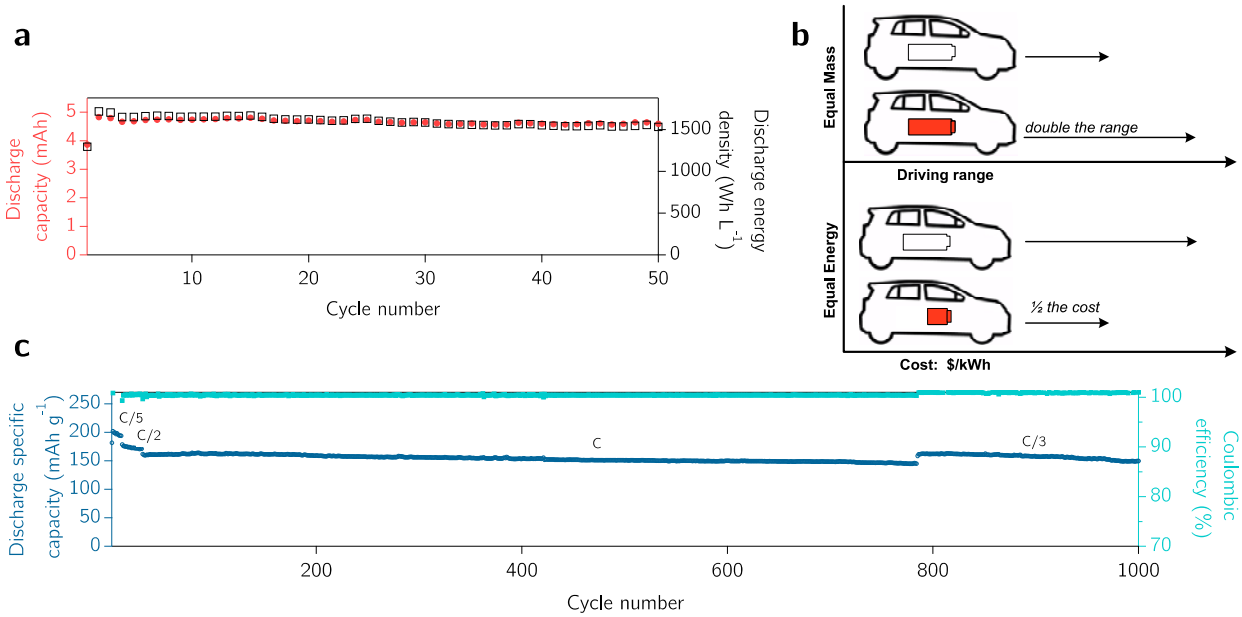

Figure 6 | Full-cell electrochemical performance of Si-cPAN/LMR system with an optimized RTIL electrolyte. (a) Specific capacities and energy density (normalized to total electrode volume) of nSi-cPAN/LMR full-cell with high mass loading (>20 mg total active material) assembled with $PYR_{13}FSI$ (1.2*M* LiFSI, 0.1*M* $LiPF_6$) electrolyte. (**b**) Animation depicting the range and cost benefits of moving to the Si/LMR electrode chemistry. (**c**) Long-term specific capacities and coulombic efficiencies of SiNW-cPAN/LMR full-cell assembled with $PYR_{13}FSI$ (1.2*M* LiFSI, 0.1*M* $LiPF_6$) electrolyte. All cycling **(a,c)** was carried out at room temperature in 2032 coin-type cells operated between 1.5 - 4.55 V (vs. Li/Li^+) with initial charges to 4.65 V (vs. Li/Li^+).

Supporting Information
for Nature Materials

In Situ Engineering of the Electrode-Electrolyte Interface for Stabilized Over-lithiated Cathodes

*Tyler Evans,[1,2] Daniela Molina Piper,[2] Huaxing Sun,[3] Timothy Porcelli,[3] Seul Cham Kim,[4] Sang Sub Han,[4] Yong Seok Choi,[4] Chixia Tian,[5] Dennis Nordlund,[6] Marca M. Doeff,[5] Chunmei Ban,[7] Sung-Jin Cho,[8] Kyu Hwan Oh,[4] and Se-Hee Lee [1,]**

Supplementary Figures

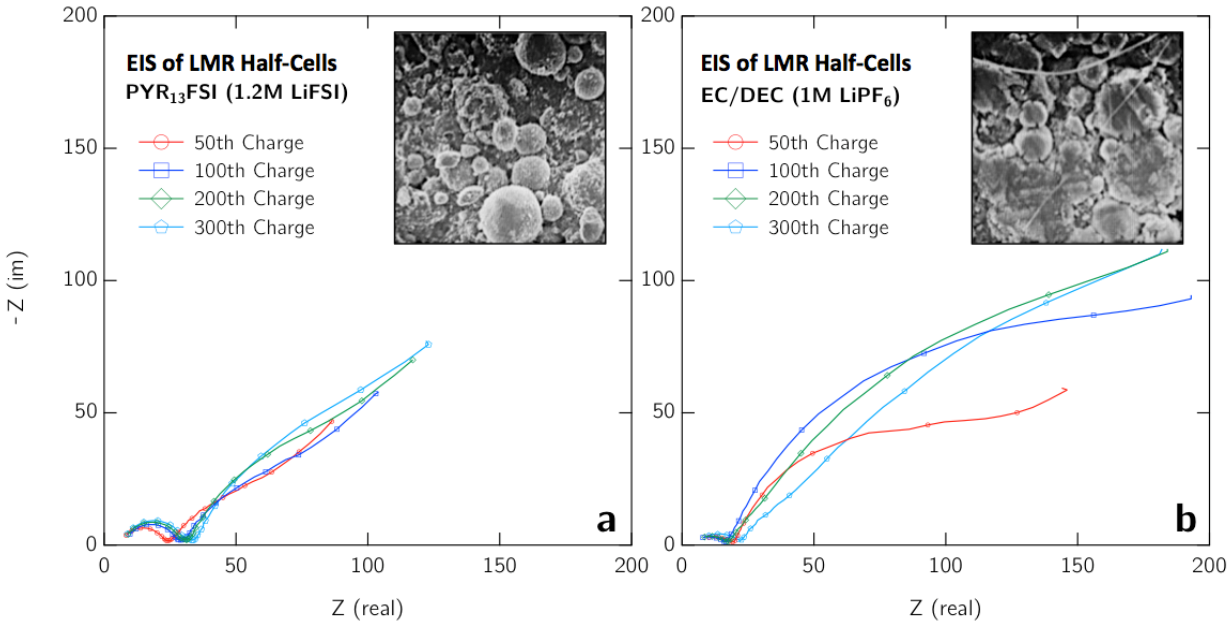

Figure S1 | Electrochemical impedance spectroscopy (EIS) spectra evolution in LMR half-cells. EIS illustrates the charge-transfer resistances found throughout the cycling of LMR half-cells in **(a)** $PYR_{13}FSI$ (1.2*M* LiFSI) electrolyte compared to **(b)** conventional electrolyte along with each of the composite morphologies after 1000 electrochemical cycles (insets).

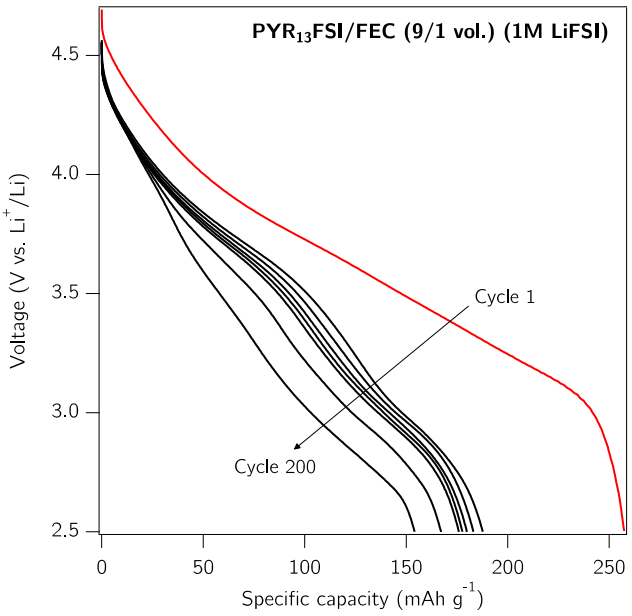

Figure S2 | Voltage fade in a LMR half-cell containing RTIL+FEC electrolyte. Voltage profiles of an LMR half-cell cycled in $PYR_{13}FSI$/FEC (9/1 vol.) (1M LiFSI) still showing severe voltage fade throughout cycling. This is attributed to the similarities between the FEC and EC molecules and the likely similar oxidative decomposition products of each.

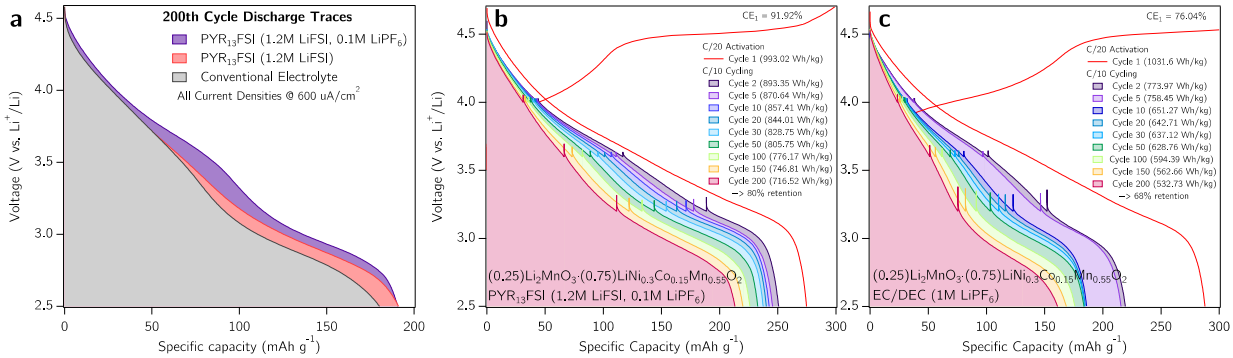

Figure S3 | Voltage fade comparison of LMR in various electrolytes. (a) 200th cycle discharge trace comparison of LMR half-cells cycled in RTIL, *m*-RTIL and EC/DEC electrolyte along with the performance comparison of the LMR material cycled in **(b)** *m*-RTIL and **(c)** EC/DEC electrolytes under ANL's "Voltage Fade Testing Protocol".

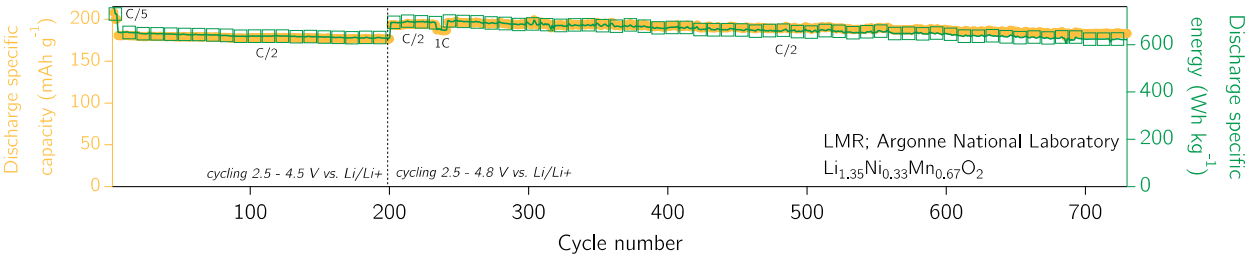

Figure S4 | Direct comparison of the LMR-mRTIL system to state-of-the-art LMR. Electrochemical performance of zero cobalt content LMR material from ANL cycled in the *m*-RTIL electrolyte demonstrating high capacities and energies with >98% retention (200 cycles) using a 4.5 V upper voltage limits (no "activation" of LMR material). The lower cut-off voltage mimics the cycling protocol used by Envia Systems. Minimal energy fade is then observed when increasing the upper voltage limit to 4.8 V, with >95% energy retention over 550 cycles following the initial 200 2.5 – 4.5 V cycles.

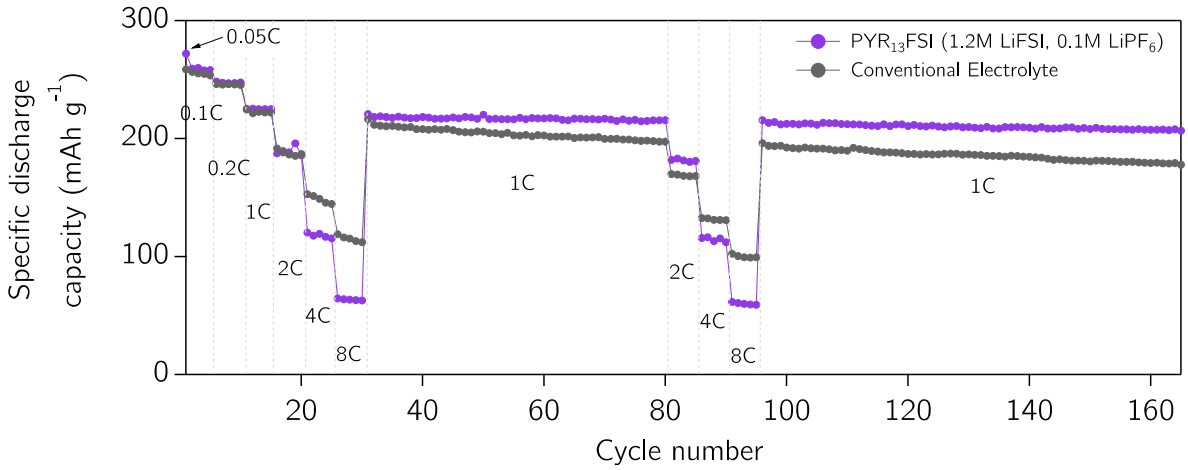

Figure S5 | LMR rate-study in *m*-RTIL vs. conventional electrolyte. Electrochemical rate study of LMR material cycled in *m*-RTIL (purple profile) and conventional organic (grey profile) electrolyte demonstrating phase stability in the *m*-RTIL electrolyte; after an initial rate test and 50 cycles at the rate of 1C, the LMR sample cycled in the *m*-RTIL electrolyte maintains its high-rate capacities while the sample cycled in conventional electrolyte shows significant capacity fade at each rate tested.

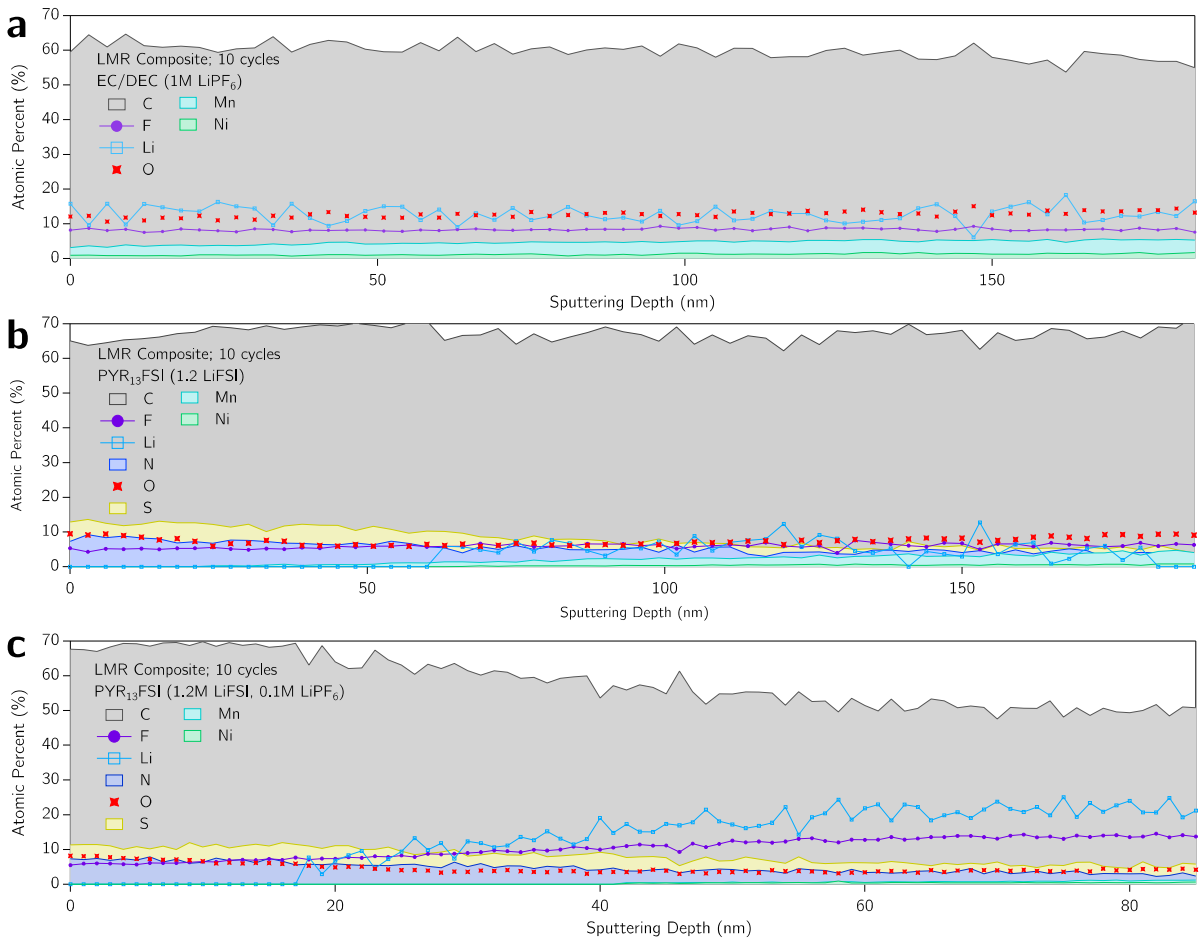

Figure S6 | CEI composition on the LMR surface after cycling in various electrolytes. XPS depth profiling highlighting elemental content in the CEI formed in (a) conventional organic, (b) RTIL, and (c) *m*-RTIL electrolytes.

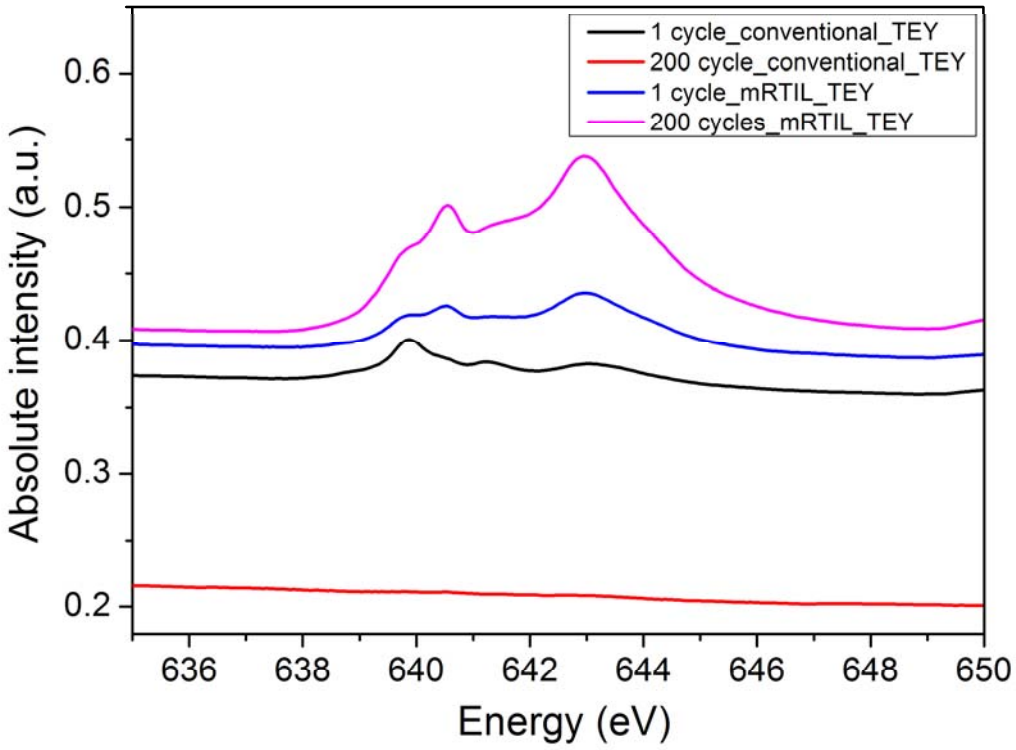

Figure S7 | Mn valence state evolution in the LMR crystal lattice. L-edge XAS (TEY mode) performed on LMR cathodes cycled up to 200 cycles shows that the average surface Mn valence state is stabilized throughout cycling in *m*-RTIL electrolytes, while the Mn ion valence state in the LMR sample cycled in conventional electrolyte is shown to shift towards lower energy (3^+) state during cycling.

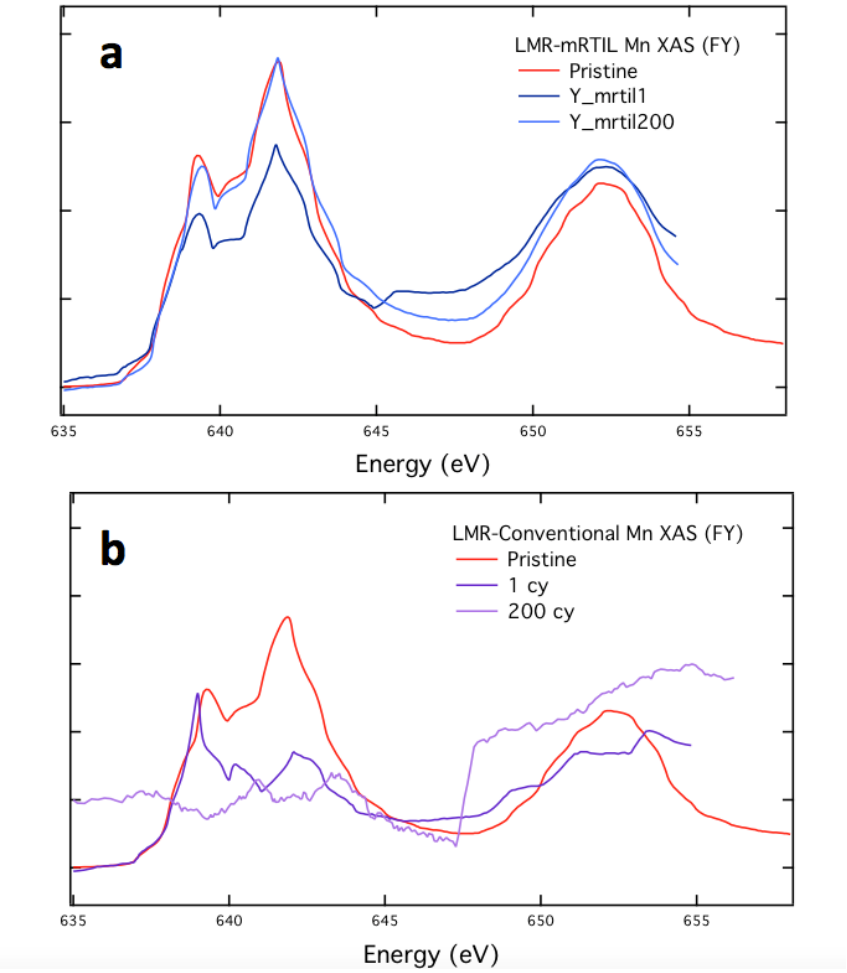

Figure S8 | Mn valence state evolution in the LMR crystal lattice. L-edge XAS (FY mode) performed on LMR cathodes cycled up to 200 cycles shows that the average surface Mn valence state is stabilized throughout cycling in **(a)** *m*-RTIL electrolytes, while the Mn ion valence state in the LMR sample cycled in **(b)** conventional electrolyte is shown to shift towards lower energy (3^{+}) state during cycling.

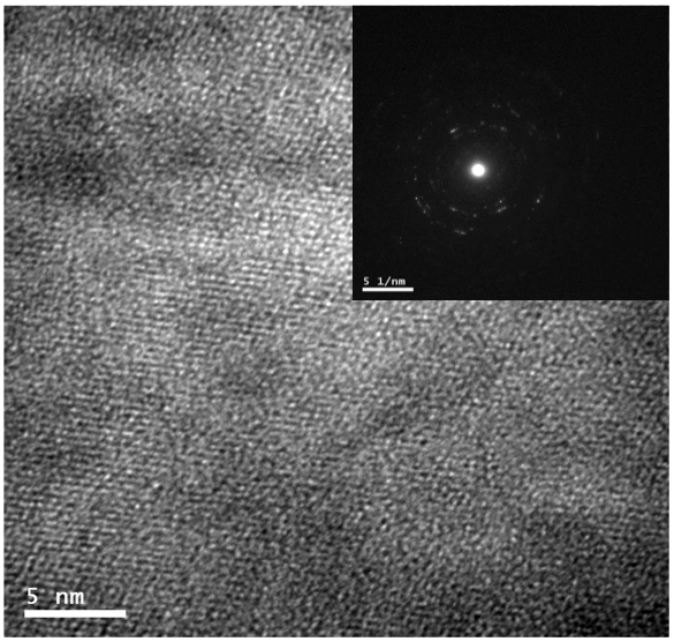

Figure S9 | Microstructure and crystallography of pristine LMR. HR-TEM micrograph of an un-cycled LMR particle showing the layered crystallography of the pristine lattice, along with Fourier transform (FFT) of the particle core.

Supplementary Methods

Electrochemical Impedance Spectroscopy. EIS was performed on LMR half-cells (Solartron 1280C) between a frequency range of 20 kHz – 10 mHz with an a.c. amplitude of 10 mV.

X-ray Absorption Spectroscopy. Prior to XAS characterization, all samples were rinsed for 5 minutes in DMC solvent to remove CEI and residue. Soft X-ray absorption spectroscopy (XAS) measurements were conducted on the bending magnet beamline 8-2 at Stanford Synchrotron Radiation Lightsource (SSRL) using a ring current of 500 mA and a 1100 l mm^{-1} spherical grating monochromator with 20 μm entrance and exit slits, providing ~0.5×10^{10} ph s^{-1} at 0.2 eV resolution in a 1 mm^2 beam spot. Data were acquired under ultrahigh vacuum (10^{-9} Torr) in a single load at room temperature using total electron yield (TEY), where the sample drain current was collected. All spectra were normalized by the current from a gold-evaporated fine grid positioned upstream of the main chamber. XAS samples were mounted on an aluminum sample holder with double-sided carbon tape in an argon-filled glove box, and they were then transferred to the load-lock chamber in a double-contained container, using a glove bag purged with argon for the transfer.